J. Astrophys. Astr. (2022) 43:7
https://doi.org/10.1007/s12036-021-09785-5

MISCELLANEOUS

Deep *V* and *I* CCD photometry of young star cluster NGC 1893 with the 3.6m DOT

NEELAM PANWAR[1,*], AMIT KUMAR[1,2] and S. B. PANDEY[1]

[1]Aryabhatta Research Institute of Observational Sciences, Manora Peak, Nainital 263001, India.
[2]School of Studies in Physics and Astrophysics, Pandit Ravishankar Shukla University, Chattisgarh 492010, India.
*Corresponding author. E-mail: neelam@aries.res.in

MS received 7 September 2021; accepted 22 October 2021

Abstract. Young star clusters consisting of massive stars are the ideal sites to study the star formation processes and influence of massive stars on the subsequent star formation. NGC 1893 is a young star cluster associated with the HII region Sh2-236. It contains about five 'O'-type stars and several early 'B'-type stars. It is located at a moderate distance of $\sim$3.25 kpc and has a reddening, $E(B-V) \sim 0.4$ mag. To characterize the young low-mass stellar population in the central portion of the cluster, we carried out deep *VI* band observations of the region using the 4K $\times$ 4K CCD IMAGER mounted on the 3.6-m Devasthal Optical Telescope. Our analysis shows that the present data are deep enough to detect stars below $V \sim 24$ mag. We found optical counterparts of $\sim$220 candidates, including young stars and unclassified cluster members from Caramazza *et al.* (2008). We estimated the membership probabilities of the Gaia sources (mostly bright stars with $G < 19$ mag) located within the cluster radius using the Gaia EDR3. Toward the fainter end, we used the optical color-magnitude diagram (CMD) to select the cluster members from a sample of young stars. The locations of young stars on the CMD show that a majority of them are low-mass stars with age <10 Myr. The unclassified candidates and X-ray sources from Caramazza *et al.* (2012) are also found to be young low-mass stars. In total, we identified $\sim$425 young stars with age <10 Myr, and 110 of these are new. Most of these stars appear as kinematic members of the cluster. By examining the CMD for the stars in the cluster region, we suggest that the cluster has insignificant contamination due to field stars in the pre-main-sequence zone of the CMD. The slope of the mass function in the mass range $0.2 \leq M/M_{\odot} \leq 2.5$ is found to be $\Gamma = -1.43 \pm 0.15$, consistent with those of other star-forming complexes. The spatial distribution of the young stars as a function of mass suggests that toward the cluster center, most of the stars are massive.

Keywords. Young star clusters: NGC 1893—stars: formation—stars: pre-main-sequence.

1. Introduction

Stars form in the molecular clouds with a variety of masses, ranging from high-mass (>8 $M_{\odot}$) to the low-mass upto 0.08 $M_{\odot}$ and most of the stars emerge as clusters (Lada & Lada 2003). Despite several observational and theoretical works focusing on the processes involved in the formation and evolution of stars and star clusters, a number of issues persist. As young star clusters possess young stars of a diverse mass range, formed from the same molecular cloud, they are particularly suited to enhance our understanding on the physical processes related to the star formation, such as, whether star formation is a fast or slow process, what is the shape of the initial mass function (IMF) towards the low-mass end, and the total star formation efficiencies. However, the presence of massive stars in such systems may significantly influence the evolution of low-mass stars and subsequent star formation. As soon as the massive stars form, they tend to ionize the natal cloud and create

This article is part of the Special Issue on "Astrophysical Jets and Observational Facilities: A National Perspective".

Published online: 31 January 2022

expanding HII region. The expanding edge of the HII region (I-front) interacts with the surrounding cloud and may trigger star formation via various processes. Thus, young star clusters associated with the HII regions and young stellar objects (YSOs) are ideal sites to study the influence of massive stars on the formation and evolution of low-mass stars and the processes involved in triggering star formation.

Observations of the early stages of star formation, i.e., Class 0/I/II YSOs show that these are associated with disk accretion, jets and outflows. However, jets and outflows are only present when a young star possesses an accretion disk. The strength of a jet depends on the evolutionary status of the driving source and the less evolved source (with thick circumstellar disk) has more powerful outflows. Hence, the presence of jets and outflows in a star-forming region can be used to identify young stars that are deeply embedded in the molecular clouds.

As YSOs possess circumstellar accretion disks during their earlier stages of formation, they also exhibit excess emission in the longer (particularly IR) wavelengths. However, the amount of excess emission depends on different evolutionary classes, i.e., Class 0, Class I, Class II and Class III (André 1995). Hence, in general, this property of the young stars is used to identify and classify them (Lada *et al.* 2006; Luhman 2012). As Class III objects are disk anemic or possess thin disks, they present no or little excess emission in infrared (IR). Therefore, IR observations become less sensitive for the identification of Class III objects. However, X-ray observations can be utilized to obtain a complete census of young stars as both Class II and Class III objects are generally more luminous in the X-ray wavelengths compared to their main-sequence (MS) counterparts (Feigelson & Montmerle 1999; Getman *et al.* 2012). Hence, IR and X-ray observations are widely used to identify and characterize a complete census of YSOs in star-forming regions.

1.1 *Our target: NGC 1893*

NGC 1893 is a young star cluster located in the Auriga OB2 association. It is associated with the HII region W8 (or Sh2-236) and contains about five 'O'-type stars and several 'B'-type stars (Marco & Negueruela 2002). Recent studies place the cluster at a moderate distance ranging from $\sim$3.2 to 3.6 kpc. Reddening, $E(B-V)$, toward the cluster direction ranges from 0.4 to 0.6 mag (Sharma *et al.* 2007; Prisinzano *et al.* 2011; Lim *et al.* 2014). The radial extent of the cluster is found to be $\sim 6'$ (Sharma *et al.* 2007). Using different color excess ratios over a wide wavelength range, Lim *et al.* (2014) found a normal reddening law ($R_V = 3.1$) towards the cluster. CO (1-0) observations of the HII region/cluster complex show that it still consists of molecular gas having $V_{\rm LSR} = (-7.2 \pm 0.5)$ km s^{-1} (Blitz *et al.* 1982). As NGC 1893 is located in the outer Galaxy and probably formed in the low-metallicity environment, it is interesting to probe how such a rich star cluster formed there despite the expected unfavorable conditions for star formation in the outer Galaxy.

The region is associated with two tadpole nebulae, Sim 129 and Sim 130, and several YSOs (Maheswar *et al.* 2007; Caramazza *et al.* 2008, 2012; Prisinzano *et al.* 2011; Lim *et al.* 2014). The spatial distribution of the YSOs shows that they have an elongated and aligned distribution from the cluster center to Sim 129 and Sim 130. An age gradient from the massive stars of the cluster toward the nebulae is also observed (Pandey *et al.* 2013; Kuhn *et al.* 2015). Lata *et al.* (2014) identified 53 young stellar variables based on the *VI* bands time-series photometric observations. They found that the rotational period of young stars decreases with stellar age and mass, and the amplitude in the light curves also declines with the same physical quantities. Based on cumulative age distribution of the classical T-Tauri stars (CTTSs) and weak-line T-Tauri stars (WTTSs), Pandey *et al.* (2013) found that these are coeval. Hence, the cluster/HII region complex is an active site of star formation and an ideal target to study the formation and evolution of the young stellar population.

Though the cluster and associated HII region is a target of various optical photometric studies, most of these were shallow ($V \sim$ 21–22 mag) and complete upto $\sim 1\ M_\odot$ (Lim *et al.* 2014). As low-mass stars out-number high-mass stars in a star cluster, information on the low-mass stellar population of the young clusters is essential to infer the cluster properties, star formation histories and mass function (MF). Deep photometric observations are important tools to probe the faint low-mass stars and study the properties of young clusters.

To characterize the low-mass stars and study star formation in the cluster region, we carried out deep *VI* band observations of the region with the 4K $\times$ 4K CCD IMAGER mounted on the 3.6-m Devasthal Optical Telescope (DOT). Our analysis shows that the

present optical data are $\sim$3 mag deeper than that of the previous studies (Sharma *et al.* 2007; Lim *et al.* 2014).

2. Observations and data reduction

The *VI* bands photometric observations of the central portion of the cluster NGC 1893 were carried out on 15 October 2020 using the 4K $\times$ 4K CCD IMAGER mounted at the axial ports of the 3.6m DOT (Pandey *et al.* 2018, Kumar *et al.* 2021). With a plate scale of $\sim$0.095 arc-sec/pixel, the CCD covers a field of view of $6.5' \times 6.5'$. The observations were carried out in a 2 $\times$ 2 binning mode to enhance the signal-to-noise ratio. The images were taken in readout noise and gain mode of 10 e^-/s and 5 e^-/ADU, respectively. The sky conditions were excellent throughout the night, and during the observations, the average full-width half-maxima (FWHM) of the point sources was $\sim 0.5''$. To avoid the saturation and contamination to the flux of the stars by the nearby bright stars, we took 12 exposures of 300 s and 210 s in both *V* and *I* bands, respectively. Thus, the total integration time for the *V* and *I* band images were 1 h and 42 min, respectively. Along with the object frames, several bias and flat frames were also taken during the same night.

Pre-processing of the object frames (i.e., bias subtraction, flat-fielding, etc.) was done using the IRAF data reduction package. We combined the *V* and *I* band images separately using the *imcombine* task of IRAF. We used the DAOPHOT-II software package (Stetson 1987) for the source detection and the photometric measurements of the detected sources in the combined images. The point-spread function (PSF) was obtained for each frame using several uncontaminated stars and the ALLSTAR task is used to obtain the instrumental magnitudes of the stars in each frame.

The instrumental magnitudes were calibrated using the photometric measurements of the stars in the cluster NGC 1893 by Sharma *et al.* (2007). For calibration, we restricted the Sharma *et al.* (2007) catalog to $18 < V\ (\mathrm{mag}) < 20$ to avoid the effects of large photometric errors and saturation of bright stars towards the fainter and brighter ends, respectively. In total, we detected about 1750 stars in both *V* and *I* bands. Out of these, about 1510 stars have magnitude uncertainty <0.1 mag in both *V* and *I* bands.

Prisinzano *et al.* (2011) also carried out optical and infrared (IR) observations of the young cluster NGC 1893 using Device Optimized for LOw RESolution, a 2K $\times$ 2K CCD camera with a plate scale of $0.25''$/pixel, mounted on the 3.6-m Telescopio Nazionale Galileo (TNG) at La Palma. They have reported seeing of $\sim 1''$ during the observations. Though our observations are performed with a similar size telescope, the excellent atmospheric conditions (FWHM $\sim 0.5''$) and better spatial resolution of 4K $\times$ 4K CCD IMAGER are the advantages. We detected sources below $V \sim 25$ mag, however considering magnitude uncertainty of <0.1 mag in both *V* and *I* bands, our photometry is limited to $V \sim 24$ mag. These values are comparable to *VI* photometry of the same region taken with the TNG (see Figures 4 and 8 of Prisinzano *et al.* 2011). Here, we note that during the observations, the reflectivity of the primary mirror of the 3.6m DOT was $\sim$60%. Hence with 90% reflectivity, we expect to reach about 0.5 mag deeper than the present observations.

Figure 1 (left panel) shows the DSS2-R band image of the cluster NGC 1893 along with the Sim 129 and Sim 130 (toward the north-east). Diamond symbols represent the locations of massive 'O'-type stars taken from SIMBAD. The square represents the area covered with the 4K $\times$ 4K CCD IMAGER observations (shown in the right panel). A color-composite image of the central portion of the cluster (FOV $\sim 6.5' \times 6.5'$) constructed using the DSS2-R (blue), 4K $\times$ 4K CCD IMAGER *V* (green) and *I*-band (red) images is shown in the right panel of Figure 1.

3. Results and discussion

3.1 *Young stellar population in the region*

The spatial distribution of the young stars traces the sites of recent/ongoing star formation. Hence, the identification and characterization of young stars in a region is essential to infer the star formation histories and the physical properties of the star clusters and HII regions. Caramazza *et al.* (2008) identified 359 YSOs in the cluster NGC 1893 using Spitzer-IRAC observations. Based on the IRAC color–color diagram and X-ray emission, these YSOs were characterized as Class 0/I, Class II or Class III sources. Out of 359 YSOs, seven sources were classified as Class 0/I, 242 Class II and 110 Class III. Caramazza *et al.* (2008) also reported $\sim$460 candidates that were not detected at 5.8 and 8.0 μm and have $[3.6] - [4.5] > 0.3$ mag. Therefore, they could not categorize these candidates as YSOs. Prisinzano *et al.* (2011) identified 1034 disk bearing (Class 0/I/II) sources

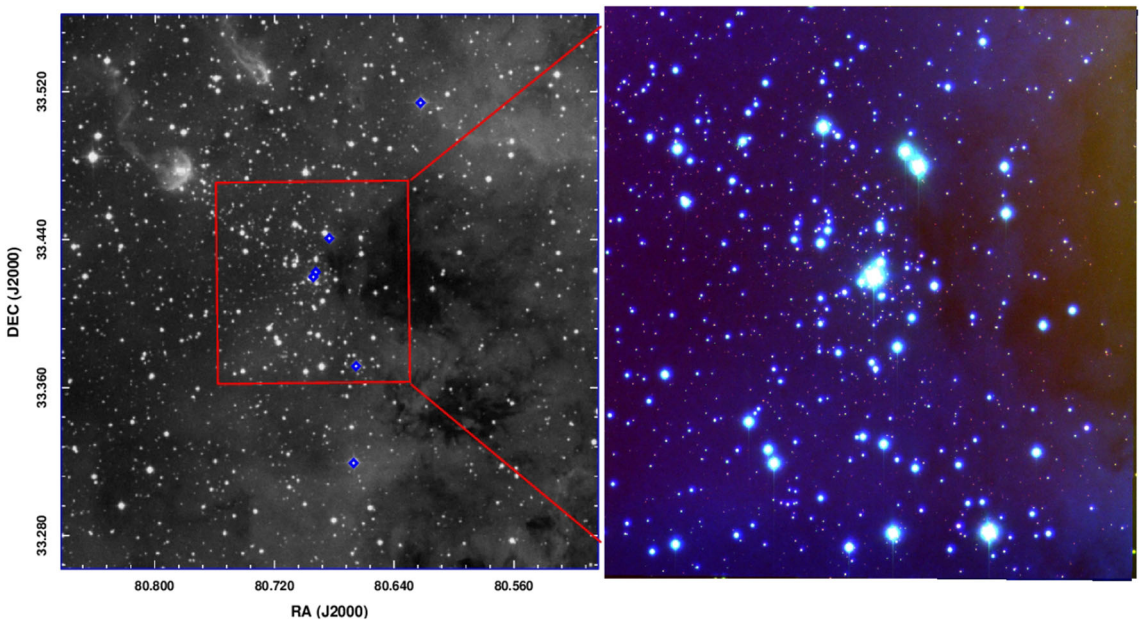

Figure 1. Left panel: DSS2-R band image of the NGC 1893 complex. Diamond symbols represent the locations of 'O' type stars in the region. Right panel: a color-composite view of the central portion ($1 \sim 6.5' \times 6.5'$ FOV) of the cluster constructed using the DSS2-R (blue), 4K × 4K CCD IMAGER *V*-band (green) and *I*-band (red) images.

and about 442 diskless (Class III) sources in the young cluster NGC 1893 by applying the Q-index method on the data of Caramazza *et al.* (2008). However, some of their YSO candidates (~ 170 sources) appeared older than the majority of the young population, which they attributed due to the edge-on disks and accretion activity. Caramazza *et al.* (2012) studied the coronal properties of the young stars in the NGC 1893 region using the Chandra X-ray observations.

3.2 *Optical counterparts of the YSOs candidates*

As young stars possess disks in their early stages and show excess emission in the longer wavelengths, the estimation of the physical properties of the young stars using longer wavelength observations can be problematic. Since optical observation mostly traces the photospheric emission from the young stars, these are the best suited to study the physical properties, such as age, mass, etc., of the young stars. In the present work, we have used the catalog of Caramazza *et al.* (2008) to guide our analysis and, in particular, to identify the young stellar population in the central portion of the cluster. We looked for the optical counterparts of the candidates (Table 4 of Caramazza *et al.* (2008)) in our optical data using a matching radius of 0.6 arc-sec. We found optical counterparts of 226 member stars within the central portion ($\sim 6.5' \times 6.5'$) of the cluster. Out of these, one source is Class 0/I candidate, whereas 106 sources are Class II and 42 sources are Class III in nature. Though the rest of the 77 sources were designated as candidates by Caramazza *et al.* (2008), these were detected in only 3.6 μm and 4.5 μm IRAC bands and hence were not identified as YSOs based on the IRAC color–color diagram. Accordingly, the nature of these sources remained ambiguous. We looked for these 77 candidates in the YSO catalog of Prisinzano *et al.* (2011) and found that 55 of these were not present in their YSO catalog either. Since we are using deep optical *VI* photometry of the cluster in the present work, it will be helpful to examine the nature of these 55 candidates of Caramazza *et al.* (2008).

We also used the catalog of X-ray sources of Caramazza *et al.* (2012) to select the additional YSO candidates in the cluster. Using a matching radius of 0.6 arc-sec, we found optical counterparts of 336 X-ray sources. Out of these, 109 sources were common to those in the catalog of Caramazza *et al.* (2008). In summary, we found that the evolutionary status of ~ 123 X-ray sources and unclassified candidates were not previously known.

3.3 *Kinematic members of the cluster NGC 1893 with Gaia EDR3*

The Gaia mission has revolutionized the kinematic studies of the stars and star clusters by providing rich

astrometric and photometric data. In the present work, we used Gaia Early Data Release 3 (EDR3; Gaia Collaboration *et al.* 2020) catalog to elucidate the kinematics of the stars in the young star cluster NGC 1893. We use Gaia EDR3 data for the sources within the cluster region (radius ≤ 6 arc-min). We used the proper motion in RA ($\mu_\alpha^\star$) and proper motion in declination (μ_δ) for the stars within the cluster radius to generate the vector point diagram (VPD), where $\mu_\alpha^\star \equiv \mu_\alpha \cos(\delta)$. We restricted only those sources with proper motion uncertainty <0.5 mas yr^{-1} and G-band magnitude uncertainty <0.1 mag. The VPD for those sources is shown in Figure 2. The over-density of sources can be easily noticed in Figure 2. The proper motion of the stars in the cluster region peaks at $\mu_\alpha^\star, \mu_\delta \sim -0.30, -1.43$ mas yr^{-1}. A circular area of radius 0.7 mas yr^{-1} around the peak of the over-density in the VPD is used to select the probable cluster members, and the remaining sources in the VPD are considered as field stars.

To determine the membership probability of the stars in the cluster region, we used the approach discussed in Pandey *et al.* (2020). Assuming a distance of $\sim$3.25 kpc (Sharma *et al.* 2007) and a radial velocity dispersion of 1 km s^{-1} for open clusters (Girard *et al.* 1989), a dispersion (σ_c) of $\sim$0.06 mas yr^{-1} in the PMs of the cluster can be expected. We calculated $\mu_{xf} = 0.84$ mas yr^{-1}, $\mu_{yf} = -2.70$ mas yr^{-1}, $\sigma_{xf} = 2.29$ mas yr^{-1} and $\sigma_{yf} = 3.76$ mas yr^{-1} for the probable field members. These values are further used to construct the frequency distributions of the cluster stars (ϕ_c^v) and field stars (ϕ_f^v) by using the equation given in Yadav *et al.* (2013) and then the value of membership probability for the ith star is calculated using the equation given below:

$$P_\mu(i) = \frac{n_c \times \phi_c^v(i)}{n_c \times \phi_c^v(i) + n_f \times \phi_f^v(i)}, \quad (1)$$

where n_c and n_f are the normalized number of probable cluster members and field members, respectively. In Figure 3 (upper panel), we have plotted the estimated membership probability for all the Gaia sources within the cluster radius as a function of G-band magnitude as blue dots. Gaia sources with high membership probability ($P_\mu > 80\%$) are shown with red circles. There seems to be a clear separation between the cluster members and field stars toward the brighter part, supporting the effectiveness of this technique. A high membership probability extends down to $G \sim 19$ mag, whereas toward the fainter limits, the probability gradually decreases. A majority of the stars with high membership probability follow a tight distribution in the VPD. From the above analysis,

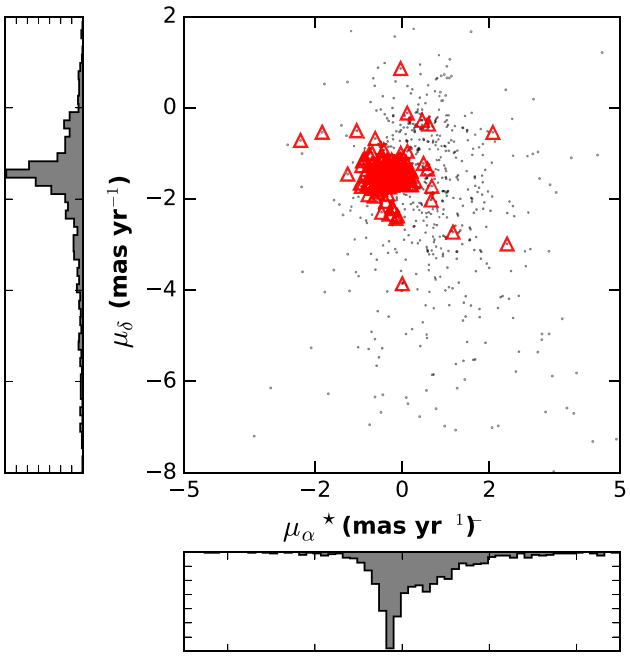

Figure 2. Proper motion vector-point diagram for the Gaia sources located within the cluster radius. The red triangles show the young stellar candidates having *VI* photometry in the present work.

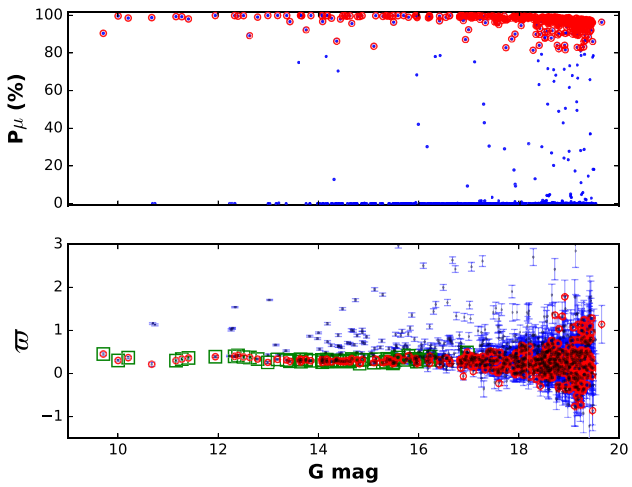

Figure 3. Top panel: membership probability for the stars located within the cluster area (radius $\sim 6'$) plotted as a function of G-band magnitude. Bottom panel: the blue dots show the distribution of parallax values for the Gaia sources within the cluster as a function of G magnitude. The error bars show respective uncertainties in the parallax values. The red circles represent the probable cluster members ($P_\mu > 80\%$). The green squares represent the probable cluster members with good parallax estimates ($\varpi/\sigma_\varpi > 5$).

we calculated the membership probability of $\sim$950 stars in the cluster region.

We also plotted the parallax for all the Gaia sources as a function of G-band magnitude (dots in Figure 3, bottom panel). The respective uncertainties in the parallax values are shown with the error bars. The red circles represent sources having membership probability $P_\mu > 80\%$. We also estimated the cluster distance using the parallax values of the cluster members having high membership probability ($P_\mu > 80\%$) and good parallax values ($\varpi/\sigma_\varpi > 5$). These sources are shown with the square symbols in Figure 3 (bottom panel). The median parallax value of these sources is 0.318 ± 0.054 mas. We estimate the cluster distance after correcting the median parallax value for the known parallax offset of ~ -0.015 (Stassun & Torres 2021). The distance estimate for the cluster using Gaia data comes out to be $\sim 3.30 \pm 0.54$ kpc, which is in agreement with that reported by Sharma *et al.* (2007).

We also cross-matched the YSOs that have counterparts in our optical photometry to sources in the Gaia catalog. Using a matching radius of $\sim$1.2 arcsec, we found $\sim$135 Gaia counterparts. These sources are shown with the red triangles in the VPD. Except for a few contaminants, most of them follow the distribution of probable cluster members in the VPD, suggesting that these YSO candidates are the cluster members.

From the above analysis, it is clear that using the Gaia EDR3 data, our sample of kinematic members of the cluster is restricted to only relatively bright members ($G < 19$ mag). Therefore, to select the candidates towards the low-mass end, we adopted the procedure discussed in the following section.

3.4 *Color-magnitude diagram: constraining young nature of the candidates*

The color-magnitude diagram (CMD) is often used to study the mass distribution and evolutionary stages of the stars of a cluster. In Figure 4 (top panel), we show the $V/(V-I)$ CMD for all the stars in our optical catalog within the cluster region. The red circles represent the cluster members with high membership probabilities ($P_\mu > 80\%$). We have also plotted a zero-age main sequence (ZAMS) isochrone (thin blue curve) from Girardi *et al.* (2002) and 1, 10 Myr pre-main-sequence (PMS) isochrones (dashed and thick curves, respectively) from Siess *et al.* (2000). In the present work, we adopted a distance of $\sim$3.25 kpc and reddening $E(B-V)$ of 0.4 mag for the cluster (Sharma *et al.* 2007). All the isochrones are corrected

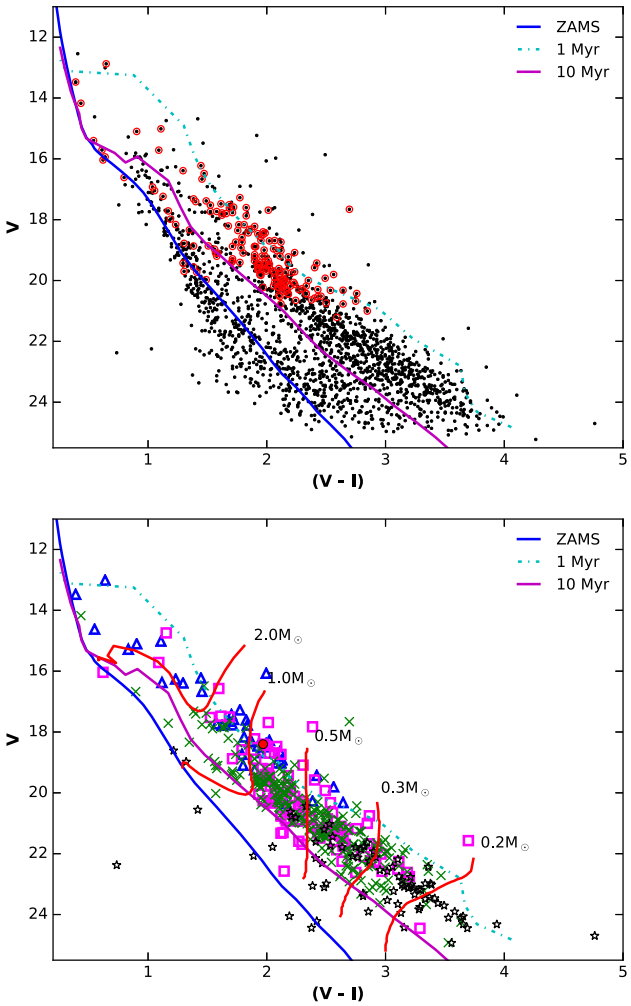

Figure 4. Top panel: $V/(V-I)$ color-magnitude diagram for the stars in the central portion of the cluster ($\sim 6.5' \times 6.5'$) obtained using the 4K $\times$ 4K CCD IMAGER observations. The open circles represent Gaia sources with $P_\mu > 80\%$. Bottom panel: $V/(V-I)$ color-magnitude diagram for the young stars in the cluster region. The red-filled circle represents the Class I object, magenta squares represent the Class II objects and blue triangles represent the Class III objects from Caramazza *et al.* (2008). Cross symbols represent the optical counterparts of the X-ray sources detected by the Chandra observations (Caramazza *et al.* 2012) that were not listed in Caramazza *et al.* (2008). Star symbols represent the candidates of the cluster from Caramazza *et al.* (2008) that were detected in only two IRAC bands and do not exhibit X-ray emission. The zero-age main sequence (Girardi *et al.* 2002) and 1, 10 Myr pre-main-sequence isochrones (Siess *et al.* 2000) corrected for the adopted distance and reddening are also plotted.

for the adopted distance and reddening. The probable cluster members (shown with red circles in the top panel of Figure 4) clearly show that most of these are young in the CMD. As can be seen, there is a clear

color gap in the cluster CMD (along the 10 Myr isochrone) that seems to separate a young stellar population (toward the right side in the CMD) from the likely field stars toward the cluster direction. A similar separation of PMS population on the CMD is also observed by Panwar *et al.* (2018) for the young cluster Berkeley 59.

There may be significant contamination by the field population along the line of sight (Sung & Bessell 2010; Sung *et al.* 2013) that can also contaminate our CMD. Therefore, to further examine the distribution of our proposed cluster population, we used the young stars selected based on the X-ray and IR emission properties from Caramazza *et al.* (2008). We constructed the $V/(V-I)$ CMD for the *Spitzer*-IRAC and Chandra X-ray identified stars (see Figure 4, bottom panel). In Figure 4 (bottom panel), the red filled circle shows the location of the Class I object, magenta squares represent the Class II objects and blue triangles represent the Class III objects from Caramazza *et al.* (2008).

By examining the locations of these YSOs in the CMD, we found that most of the YSOs are located to the right of the 10 Myr PMS isochrone of Siess *et al.* (2000), confirming that the contamination due to field stars in the PMS population of the cluster region is insignificant. A majority of the YSOs selected based on the IR and X-ray properties by Caramazza *et al.* (2008) are young low-mass stars.

To examine the evolutionary status of the ambiguous candidates (without 5.8 and 8.0 μm photometry) of the Caramazza *et al.* (2008) and X-ray sources from Caramazza *et al.* (2012), we placed these sources on the optical CMD. In Figure 4 (bottom panel), cross symbols represent the optical counterparts of the X-ray sources detected by the Chandra observations (Caramazza *et al.* 2012) that were not cataloged by Caramazza *et al.* (2008) as YSOs. In contrast, the star symbols represent the ambiguous candidates of NGC 1893 cataloged in Table 4 by Caramazza *et al.* (2008). The positions of these sources on the optical CMD suggest that a majority of them are young low-mass stars. The positions of these young stars along with the V and I band magnitudes are listed in Table 1.

Comparing the distribution of all stars with the *Spitzer* and X-ray identified YSOs in the $V/(V-I)$ CMD, we suggest that the stars located toward the right of the 10 Myr isochrone may belong to the PMS population of the cluster NGC 1893. However, deep optical observations of a nearby control field or spectroscopic observations of the PMS population are necessary for the confirmation.

Table 1. Positions and photometric magnitudes of new YSO candidates.

Id	$\alpha_{(2000)}$	$\delta_{(2000)}$	$V \pm eV$	$I \pm eI$
1	80.65629	33.36719	24.45 ± 0.18	20.76 ± 0.04
2	80.73150	33.37947	23.53 ± 0.08	20.52 ± 0.04
3	80.65462	33.38117	24.93 ± 0.31	21.38 ± 0.11
4	80.65742	33.37886	23.75 ± 0.10	20.46 ± 0.03
5	80.73238	33.42503	23.08 ± 0.06	19.87 ± 0.02
6	80.64283	33.38447	22.43 ± 0.03	19.07 ± 0.02
7	80.75638	33.42536	22.43 ± 0.03	19.37 ± 0.02
8	80.69583	33.39625	21.77 ± 0.02	18.95 ± 0.01
9	80.65854	33.40050	23.63 ± 0.09	20.19 ± 0.03
10	80.74296	33.37753	22.15 ± 0.03	19.74 ± 0.02
11	80.69575	33.43133	22.75 ± 0.05	19.63 ± 0.02
12	80.70321	33.42994	22.88 ± 0.04	19.74 ± 0.02
13	80.64454	33.43739	21.73 ± 0.02	19.20 ± 0.02
14	80.71604	33.44136	24.32 ± 0.15	20.67 ± 0.03
15	80.72604	33.42392	23.23 ± 0.06	20.16 ± 0.02
16	80.74096	33.45031	23.83 ± 0.10	20.55 ± 0.04
17	80.69533	33.36542	22.09 ± 0.02	19.37 ± 0.02
18	80.70000	33.44533	20.81 ± 0.01	18.57 ± 0.01
19	80.69396	33.44772	22.76 ± 0.04	19.55 ± 0.02
20	80.68996	33.44886	21.20 ± 0.02	18.72 ± 0.01
21	80.73087	33.44939	24.11 ± 0.13	20.48 ± 0.03
22	80.72146	33.45006	22.24 ± 0.03	19.38 ± 0.02
23	80.65863	33.45064	23.40 ± 0.08	20.58 ± 0.04
24	80.75554	33.46075	22.32 ± 0.03	19.85 ± 0.02
25	80.67600	33.45364	23.09 ± 0.06	19.93 ± 0.03
26	80.72067	33.46458	23.43 ± 0.07	20.06 ± 0.03
27	80.68438	33.41661	20.44 ± 0.01	18.11 ± 0.01
28	80.69267	33.45094	23.02 ± 0.06	19.63 ± 0.02
29	80.72354	33.42625	23.71 ± 0.10	20.21 ± 0.03
30	80.71304	33.46053	23.90 ± 0.14	20.32 ± 0.03
31	80.63804	33.46564	21.61 ± 0.03	19.20 ± 0.02
32	80.69742	33.46828	23.49 ± 0.11	20.16 ± 0.03
33	80.68633	33.38081	24.43 ± 0.18	21.27 ± 0.07
34	80.72071	33.38917	23.47 ± 0.08	20.05 ± 0.03
35	80.68033	33.40683	24.32 ± 0.19	20.39 ± 0.03
36	80.71533	33.40808	24.06 ± 0.13	20.41 ± 0.03
37	80.73371	33.41489	22.19 ± 0.02	19.08 ± 0.01
38	80.70925	33.40958	23.03 ± 0.06	19.89 ± 0.02
39	80.71037	33.41331	23.66 ± 0.10	20.55 ± 0.03
40	80.67242	33.42939	21.02 ± 0.02	18.50 ± 0.01
41	80.69050	33.43528	23.31 ± 0.07	20.49 ± 0.04
42	80.68492	33.43072	23.11 ± 0.07	19.88 ± 0.02
43	80.73079	33.44306	23.13 ± 0.06	19.94 ± 0.02
44	80.70250	33.44439	21.86 ± 0.02	19.06 ± 0.01
45	80.65404	33.37956	23.95 ± 0.14	20.82 ± 0.05
46	80.71221	33.36967	19.96 ± 0.01	17.82 ± 0.01
47	80.70875	33.44600	21.99 ± 0.06	19.00 ± 0.02
48	80.70008	33.36347	18.88 ± 0.01	16.98 ± 0.01
49	80.70225	33.40778	19.80 ± 0.01	17.59 ± 0.01
50	80.67783	33.41528	22.42 ± 0.04	19.57 ± 0.02
51	80.73717	33.44658	22.15 ± 0.03	19.26 ± 0.02

Table 1. Continued.

Id	$\alpha_{(2000)}$	$\delta_{(2000)}$	$V \pm eV$	$I \pm eI$
52	80.68675	33.41978	22.42 ± 0.04	19.73 ± 0.02
53	80.68450	33.41511	21.30 ± 0.02	18.81 ± 0.01
54	80.69863	33.44711	20.77 ± 0.01	18.13 ± 0.01
55	80.74375	33.44139	23.61 ± 0.08	20.66 ± 0.04
56	80.69458	33.39606	22.87 ± 0.05	19.85 ± 0.02
57	80.71696	33.44383	23.10 ± 0.05	20.21 ± 0.03
58	80.72688	33.43981	22.68 ± 0.05	20.06 ± 0.03
59	80.70908	33.44658	18.97 ± 0.01	17.41 ± 0.01
60	80.73842	33.44344	21.17 ± 0.02	18.72 ± 0.01
61	80.68525	33.42400	23.06 ± 0.05	20.10 ± 0.03
62	80.68050	33.44478	22.40 ± 0.03	19.52 ± 0.02
63	80.68983	33.41750	21.68 ± 0.02	18.75 ± 0.01
64	80.69846	33.41500	21.70 ± 0.02	18.97 ± 0.01
65	80.70829	33.41067	20.86 ± 0.02	18.37 ± 0.01
66	80.70017	33.41553	20.31 ± 0.01	18.14 ± 0.01
67	80.69579	33.42458	20.04 ± 0.01	17.94 ± 0.01
68	80.70346	33.42611	19.88 ± 0.01	17.81 ± 0.01
69	80.71450	33.41242	20.53 ± 0.01	18.42 ± 0.01
70	80.68837	33.40383	22.59 ± 0.07	19.41 ± 0.02
71	80.69200	33.43078	19.43 ± 0.02	17.53 ± 0.01
72	80.71504	33.40528	21.51 ± 0.02	19.08 ± 0.01
73	80.70096	33.41422	22.14 ± 0.03	19.11 ± 0.01
74	80.71096	33.44517	20.65 ± 0.01	18.41 ± 0.01
75	80.72900	33.42025	20.06 ± 0.01	17.91 ± 0.01
76	80.69771	33.42211	19.71 ± 0.01	17.65 ± 0.01
77	80.68375	33.39275	22.75 ± 0.04	20.14 ± 0.03
78	80.70804	33.42825	17.89 ± 0.01	16.35 ± 0.01
79	80.70304	33.37025	21.33 ± 0.02	18.85 ± 0.01
80	80.70808	33.44975	19.61 ± 0.02	17.50 ± 0.01
81	80.75825	33.45269	23.20 ± 0.07	20.34 ± 0.03
82	80.70363	33.46756	22.68 ± 0.05	19.91 ± 0.02
83	80.68200	33.37367	23.22 ± 0.07	19.90 ± 0.02
84	80.68908	33.39406	23.13 ± 0.06	20.14 ± 0.03
85	80.69333	33.39747	21.93 ± 0.02	18.92 ± 0.01
86	80.74046	33.45139	24.93 ± 0.27	21.40 ± 0.07
87	80.68050	33.45406	22.89 ± 0.05	20.09 ± 0.03
88	80.69779	33.45925	22.97 ± 0.06	20.06 ± 0.02
89	80.74229	33.44472	18.74 ± 0.04	17.00 ± 0.01
90	80.69917	33.43533	22.44 ± 0.04	19.44 ± 0.05
91	80.71362	33.41425	22.92 ± 0.05	20.22 ± 0.03
92	80.74192	33.43458	21.00 ± 0.02	18.70 ± 0.02
93	80.69258	33.42667	20.86 ± 0.04	18.57 ± 0.01
94	80.71742	33.43439	22.40 ± 0.04	19.73 ± 0.02
95	80.71613	33.42244	22.28 ± 0.03	19.74 ± 0.02
96	80.70333	33.43089	20.87 ± 0.01	18.27 ± 0.01
97	80.73067	33.43503	21.46 ± 0.02	18.96 ± 0.01
98	80.67933	33.44217	19.81 ± 0.01	17.87 ± 0.01
99	80.74229	33.44506	20.02 ± 0.02	17.86 ± 0.01
100	80.69483	33.43578	23.22 ± 0.06	20.21 ± 0.03
101	80.69554	33.44658	24.25 ± 0.19	20.62 ± 0.04
102	80.67579	33.46319	23.33 ± 0.09	20.53 ± 0.04
103	80.65292	33.43331	22.72 ± 0.05	19.25 ± 0.02
104	80.69171	33.42394	18.96 ± 0.02	16.90 ± 0.01
105	80.68162	33.44603	20.76 ± 0.01	18.30 ± 0.01
106	80.68975	33.42769	18.88 ± 0.01	16.98 ± 0.01
107	80.71637	33.44664	22.21 ± 0.04	19.52 ± 0.02
108	80.71179	33.42675	21.53 ± 0.05	18.89 ± 0.01
109	80.69796	33.42717	22.94 ± 0.05	19.77 ± 0.02
110	80.69467	33.42525	20.74 ± 0.02	18.24 ± 0.01

3.5 *Mass function of the young stars*

The distribution of the stellar masses in a star cluster at a star formation event is termed as the IMF of that star cluster. Young star clusters (age <10 Myr) are particularly suited for IMF studies. They are too young to lose a significant number of members either due to dynamical evolution or stellar evolution. Hence, their MFs can be considered IMFs. The variation of the MF is an important tool that gives clues to the physical conditions of star formation processes (Bate 2009). The MF is defined as the number of stars per unit logarithmic mass interval and is generally represented by a power-law with a slope,

$$\Gamma = d\log N(\log m)/d\log m,$$

where $N(\log m)$ is the distribution of the number of stars per unit logarithmic mass interval. Observational results for most of the star clusters in the solar neighborhood suggest MF slopes similar to that given by Salpeter (1955), that is, $\Gamma = -1.35$.

Here, we used the optical CMD to count the number of stars in different mass bins, which is shown in the lower panel of Figure 4 along with isochrones and evolutionary tracks. Since our YSO sample is complete down to 0.2 $M_{\odot}$, for the MF study we have taken only those YSOs that have masses in the range of $0.2 \leq M/M_{\odot} \leq 2.5$. The mass distribution of our YSO sample has a best-fitting slope, $\Gamma = -1.43 \pm 0.15$ (see Figure 5), similar to the Salpeter value. Our YSO MF appears consistent with those reported for other active star-forming regions, e.g., the MF of a YSO sample (with masses >0.2 $M_{\odot}$) derived by Erickson *et al.* (2011), the YSO MF slopes of the star-forming regions W51 A ($\Gamma = -1.17 \pm 0.26$) and W51 B ($\Gamma = -1.32 \pm 0.26$) by Kang *et al.* (2009) and the YSO MF slope of the young cluster IC 1805 ($\Gamma = -1.23 \pm 0.14$) derived by Panwar *et al.* (2017).

The MF slope below ~ 1 $M_{\odot}$ shows a flattening. It has already been pointed out earlier by many groups

(Kroupa 2002; Chabrier 2003, 2005; Ojha *et al.* 2009; Damian *et al.* 2021) that for the masses above $\sim 1\ M_{\odot}$, the MF can generally be approximated by a declining power-law with a slope similar to the Salpeter, whereas for the masses below $\sim 1\ M_{\odot}$ the distribution becomes flatter, and turns down at the lowest stellar masses.

3.6 *Indication for the mass segregation*

Although there are extensive studies on mass segregation in star clusters, only a few focused on the mass segregation among low-mass stars (Andersen *et al.* 2011; Panwar *et al.* 2018). Sharma *et al.* (2007) studied the mass segregation in the young cluster NGC 1893 in the mass range $5.5 \leq M/M_{\odot} \leq 17.7$ and found that the high-mass stars are more centrally concentrated than their lower-mass siblings. In the present work, we investigated the mass segregation in low-mass stars by dividing our low-mass young stars, that are located within the 3 arc-min radius around the cluster center, into two mass groups, $0.2 \leq M/M_{\odot} \leq 0.5$ and $0.5 \leq M/M_{\odot} \leq 2.5$. Figure 6 (left panel) shows the spatial distribution of the stars from these two different groups. Toward the center of the cluster, most of the YSOs seem to be relatively massive. The cumulative distribution of the young stars as a function of radial distance from the cluster center in two different mass groups (see Figure 6, right panel) also suggest that more massive stars ($0.5 \leq M/M_{\odot} \leq 2.5$) tend to lie toward the cluster center, which indicates the mass segregation in the central portion of the cluster region. As the estimated relaxation time for the cluster is very large compared to the age of the cluster, the observed mass segregation in the cluster may be primordial in nature.

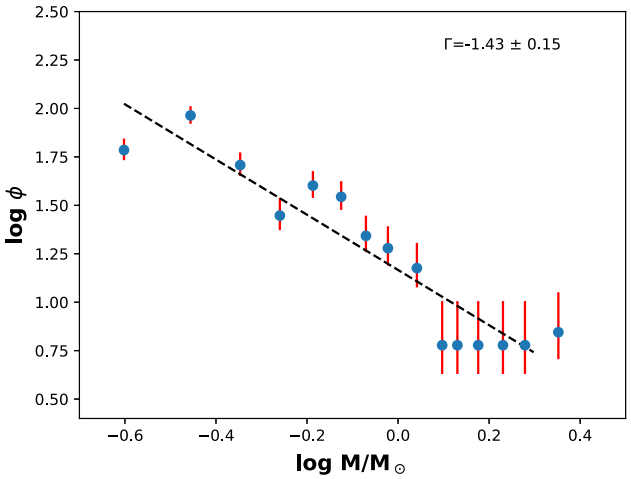

Figure 5. The MF of the YSOs in the mass range ($0.2 \leq M/M_{\odot} \leq 2.5$), derived from the optical data. The error bars represent $\pm\sqrt{N}$ errors. The dashed line shows the least-squares fit to the mass ranges described in the text. The value of the slope obtained is given in the figure.

4. Summary and conclusions

Here, we present the results of our deep optical (*VI*) observations of the central portion of the cluster NGC 1893. Thanks to the excellent observing conditions and spatial resolution of 4K × 4K CCD IMAGER, present data are ~ 3 mag deeper than most of the previous studies.

- Considering a distance of ~ 3.25 kpc and reddening $E(B-V)$ of ~ 0.4 mag for the cluster, our optical data are deep enough to reveal the stars below $\sim 0.2\ M_{\odot}$.

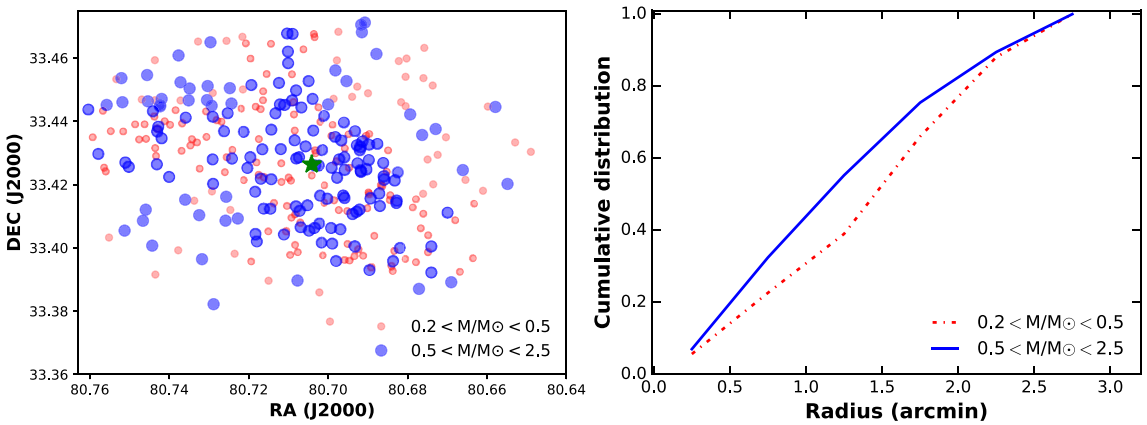

Figure 6. Left panel: spatial distribution of the YSO candidates within the 3 arc-min radius around the cluster center (shown with a green star symbol). Right panel: cumulative radial distribution of the young stars in two mass bins.

- We found counterparts of $\sim$450 YSO, candidates and X-ray sources in our optical catalog.
- We estimated the membership probability of the stars in the cluster region using the Gaia EDR3. The parallax values of the stars with high membership probability and good parallax measurements ($\varpi/\sigma_{\varpi} > 5$) are used to estimate the cluster distance. The estimated distance of $\sim$3.30 kpc is in good agreement with the photometric distance estimate for the cluster reported by Sharma *et al.* (2007).
- The locations of the young stellar candidates in the $V/(V-I)$ CMD show that most of them have ages <10 Myr. Comparing the CMDs for all stars and young members in the cluster region, we suggest an insignificant contribution of the field stars in the PMS zone of the cluster CMD and the young stellar population of the cluster region can be identified using the CMD.
- We also found that most of the candidates having no classification flag in Caramazza *et al.* (2008) and X-ray sources in Caramazza *et al.* (2012) also occupy the locations of PMS stars in CMD.
- Based on the present optical observations, we identified $\sim$425 young stars in the central portion of the cluster NGC 1893 and $\sim$110 of these were new. Our results also demonstrate that present optical *VI* observations with the 4K $\times$ 4K CCD IMAGER reveal faint low-mass stars ($V \sim 25$ mag at 60% reflectivity of the primary mirror) in the cluster NGC 1893.
- The MF of our YSO sample has a power-law index of -1.43 ± 0.15, close to the Salpeter value (-1.35) and reported for other star-forming regions. The spatial distribution of the YSOs as a function of mass suggests that toward the cluster center, most of the stars are relatively massive.

Acknowledgments

The authors would like to thank the referee for the valuable comments that significantly improved the manuscript. Also thankful to the DTAC and staff of the 3.6-m DOT which is operated by ARIES. This work has made use of data from the European Space Agency (ESA) mission *Gaia* (https://www.cosmos.esa.int/gaia), processed by the *Gaia* Data Processing and Analysis Consortium (DPAC, https://www.cosmos.esa.int/web/gaia/dpac/consortium). Funding for the DPAC has been provided by national institutions, in particular, the institutions participating in the *Gaia* Multilateral Agreement.

References

André P. 1995, Ap&SS, 224, 29
Andersen M., Meyer M. R., Robberto M., Bergeron L. E., Reid N. 2011, A&A, 534, A10
Bate M. R. 2009, MNRAS, 392, 1363
Blitz L., Fich M., Stark A. A. 1982, ApJS, 49, 183
Caramazza M., Micela G., Prisinzano L., Rebull L., Sciortino S., Stauffer J. R. 2008, A&A, 488, 211
Caramazza M., *et al.* 2012, A&A, 539, A74
Chabrier G. 2003, PASP, 115, 763
Chabrier G. 2005, in Corbelli E., Palla F., Zinnecker H., eds, Astrophysics and Space Science Library, Vol. 327, The Initial Mass Function 50 Years Later. Springer, Dordrecht, p. 41
Damian B., Jose J., Samal M. R., Moraux E., Das S. R., Patra S. 2021, MNRAS, 504, 2557
Feigelson E. D., Montmerle T. 1999, ARA&A, 37, 363
Gaia Collaboration 2020, VizieR Online Data Catalog, I/350
Getman K. V., Feigelson E. D., Sicilia-Aguilar A., Broos P. S., Kuhn M. A., Garmire G. P. 2012, MNRAS, 426, 2917
Girard T. M., Grundy W. M., Lopez C. E., Van Altena W. F. 1989, AJ, 98, 227
Girardi L., *et al.* 2002, A&A, 391, 195
Kroupa P. 2002, Science, 295, 82
Kuhn M. A., Getman K. V., Feigelson E. D. 2015, ApJ, 802, 60
Kumar Ł A., Pandey S. B., Singh A.Ł. *et al.* 2021, arXiv: 2111.13018
Lada C. J., Lada E. A. 2003, ARA&A, 41, 57
Lada C. J., Muench A. A., Luhman K. L., *et al.* 2006, AJ, 131, 1574
Lata *et al.* 2014, MNRAS, 442, 273
Lim B., Sung H., Kim J. S., Bessell M. S., Park B. G. 2014, MNRAS, 443, 454
Luhman K. L. 2012, ARA&A, 50, 65
Maheswar G., Sharma S., Biman J. M., Pandey A. K., Bhatt H. C. 2007, MNRAS, 379, 123
Marco A., Negueruela I. 2002, A&A, 393, 195
Ojha D. K., Tamura M., Nakajima Y., *et al.* 2009, ApJ, 693, 634
Pandey A. K., Samal M. R., Chauhan N., *et al.* 2013, New Astron., 19, 1
Pandey S. B., Yadav R. K. S., Nanjappa N., 2018, BSRSL, 87, 42
Pandey R., Sharma S., Panwar N., *et al.* 2020, ApJ, 891, 81

Panwar N., Samal M. R., Pandey A. K., *et al.* 2017, MNRAS, 468, 2684
Panwar N., Pandey A. K., Samal M. R., *et al.* 2018, AJ, 155, 44
Prisinzano L., Sanz-Forcada J., Micela G., *et al.* 2011, A&A, 527, 19
Salpeter E. E. 1955, ApJ, 121, 161
Sharma S., Pandey A. K., Ojha D. K., *et al.* 2007, MNRAS, 380, 1141
Siess L., Dufour E., Forestini M., 2000, A&A, 358, 5931
Stassun K. G., Torres G. 2021, ApJ, 907, 33
Yadav R. K. S., Sariya D. P., Sagar R. 2013, MNRAS, 430, 3350